Efficiency of the topological signature in the NEXT-White detector

The NEXT Collaboration

P. Ferrario,[15,9,a] J.M. Benlloch-Rodríguez,[18] G. Díaz,[15,20] M. Kekic,[18] J.A. Hernando Morata,[20] J. Renner,[18] A. Usón,[18] J.J. Gómez-Cadenas,[15,9,b] C. Adams,[11] V. Álvarez,[18] L. Arazi,[6] I.J. Arnquist,[19] C.D.R Azevedo,[4] K. Bailey,[2] F. Ballester,[21] F.I.G.M. Borges,[13] S. Cárcel,[18] J.V. Carrión,[18] S. Cebrián,[22] E. Church,[19] C.A.N. Conde,[13] J. Díaz,[18] M. Diesburg,[5] J. Escada,[13] R. Esteve,[21] R. Felkai,[18] A.F.M. Fernandes,[12] L.M.P. Fernandes,[12] A.L. Ferreira,[4] E.D.C. Freitas,[12] J. Generowicz,[15] A. Goldschmidt,[8] D. González-Díaz,[20] R. Guenette,[11] R.M. Gutiérrez,[10] J. Haefner,[11] K. Hafidi,[2] J. Hauptman,[1] C.A.O. Henriques,[12] P. Herrero,[15,18] V. Herrero,[21] Y. Ifergan,[6,7] S. Johnston,[2] B.J.P. Jones,[3] M.R. Jorge,[12] L. Labarga,[17] A. Laing,[3] P. Lebrun,[5] N. López-March,[18] M. Losada,[10] R.D.P. Mano,[12] J. Martín-Albo,[11] A. Martínez,[15] G. Martínez-Lema,[18,20] A.D. McDonald,[3] F. Monrabal,[15] C.M.B. Monteiro,[12] F.J. Mora,[21] J. Muñoz Vidal,[18] P. Novella,[18] D.R. Nygren,[3,c] B. Palmeiro,[18] A. Para,[5] J. Pérez,[18,d] F. Psihas,[3] M. Querol,[18] J. Repond,[2] S. Riordan,[2] L. Ripoll,[16] Y. Rodriguez Garcia,[10] J. Rodríguez,[21] L. Rogers,[3] B. Romeo,[15] C. Romo-Luque,[18] F.P. Santos,[13] J.M.F. dos Santos,[12] A. Simón,[6] C. Sofka,[14,e] M. Sorel,[18] T. Stiegler,[14] J.F. Toledo,[21] J. Torrent,[15] J.F.C.A. Veloso,[4] R. Webb,[14] R. Weiss-Babai,[6,f] J.T. White,[14,g] K. Woodruff,[3] N. Yahlali[18]

[1] *Department of Physics and Astronomy, Iowa State University, 12 Physics Hall, Ames, IA 50011-3160, USA*

[2] *Argonne National Laboratory, Argonne, IL 60439, USA*

[3] *Department of Physics, University of Texas at Arlington, Arlington, TX 76019, USA*

[4] *Institute of Nanostructures, Nanomodelling and Nanofabrication (i3N), Universidade de Aveiro, Campus de Santiago, Aveiro, 3810-193, Portugal*

[5] *Fermi National Accelerator Laboratory, Batavia, IL 60510, USA*

[6] *Nuclear Engineering Unit, Faculty of Engineering Sciences, Ben-Gurion University of the Negev, P.O.B. 653, Beer-Sheva, 8410501, Israel*

[7] *Nuclear Research Center Negev, Beer-Sheva, 84190, Israel*

[8] *Lawrence Berkeley National Laboratory (LBNL), 1 Cyclotron Road, Berkeley, CA 94720, USA*

[9] *Ikerbasque, Basque Foundation for Science, Bilbao, E-48013, Spain*

[a] Corresponding author.

[b] NEXT Co-spokesperson.

[c] NEXT Co-spokesperson.

[d] Now at Laboratorio Subterráneo de Canfranc, Spain.

[e] Now at University of Texas at Austin, USA.

[f] On leave from Soreq Nuclear Research Center, Yavneh, Israel.

[g] Deceased.

[10] *Centro de Investigación en Ciencias Básicas y Aplicadas, Universidad Antonio Nariño, Sede Circunvalar, Carretera 3 Este No. 47 A-15, Bogotá, Colombia*
[11] *Department of Physics, Harvard University, Cambridge, MA 02138, USA*
[12] *LIBPhys, Physics Department, University of Coimbra, Rua Larga, Coimbra, 3004-516, Portugal*
[13] *LIP, Department of Physics, University of Coimbra, Coimbra, 3004-516, Portugal*
[14] *Department of Physics and Astronomy, Texas A&M University, College Station, TX 77843-4242, USA*
[15] *Donostia International Physics Center (DIPC), Paseo Manuel Lardizabal, 4, Donostia-San Sebastian, E-20018, Spain*
[16] *Escola Politècnica Superior, Universitat de Girona, Av. Montilivi, s/n, Girona, E-17071, Spain*
[17] *Departamento de Física Teórica, Universidad Autónoma de Madrid, Campus de Cantoblanco, Madrid, E-28049, Spain*
[18] *Instituto de Física Corpuscular (IFIC), CSIC & Universitat de València, Calle Catedrático José Beltrán, 2, Paterna, E-46980, Spain*
[19] *Pacific Northwest National Laboratory (PNNL), Richland, WA 99352, USA*
[20] *Instituto Gallego de Física de Altas Energías, Univ. de Santiago de Compostela, Campus sur, Rúa Xosé María Suárez Núñez, s/n, Santiago de Compostela, E-15782, Spain*
[21] *Instituto de Instrumentación para Imagen Molecular (I3M), Centro Mixto CSIC - Universitat Politècnica de València, Camino de Vera s/n, Valencia, E-46022, Spain*
[22] *Laboratorio de Física Nuclear y Astropartículas, Universidad de Zaragoza, Calle Pedro Cerbuna, 12, Zaragoza, E-50009, Spain*

E-mail: paola.ferrario@dipc.org

Abstract: In experiments searching for neutrinoless double-beta decay, the possibility of identifying the two emitted electrons is a powerful tool in rejecting background events and therefore improving the overall sensitivity of the experiment. In this paper we present the first measurement of the efficiency of a cut based on the different event signatures of double and single electron tracks, using the data of the NEXT-White detector, the first detector of the NEXT experiment operating underground. Using a ^{228}Th calibration source to produce signal-like and background-like events with energies near 1.6 MeV, a signal efficiency of 73.7 ± 5.0 (fit)% for a background acceptance of 21.6 ± 1.3 (fit)% is found, in excellent agreement with Monte Carlo simulations. An extrapolation to the energy region of the neutrinoless double beta decay by means of Monte Carlo simulations is also carried out, and the results obtained show a slight improvement over those obtained at lower energies.

Contents

1 Topological signature in $\beta\beta0\nu$ searches using high pressure xenon TPCs

Neutrinoless double beta decay ($\beta\beta0\nu$) is an unobserved decay, in which two neutrons convert into protons with the emission of two electrons and no antineutrinos. The observation of this decay would imply lepton number violation and the demonstration of the Majorana nature of neutrinos. A Majorana neutrino could be one of the necessary elements to generate the matter-antimatter asymmetry of the Universe, via leptogenesis [1].

A large experimental effort is currently ongoing to discover $\beta\beta0\nu$ in several isotopes and using different experimental techniques, which try to maximize two main requirements, namely excellent energy resolution and background rejection power. The NEXT experiment uses a high pressure time projection chamber with electroluminescence amplification, to search for $\beta\beta0\nu$ in the isotope 136 of xenon.

The Time Projection Chamber (TPC) is one of the most widely used detectors in particle physics; in the last decade, its use has grown among the experiments that search for rare events, such as dark matter or neutrinoless double beta decay [2, 3]. One of the advantages of gaseous TPCs, compared to liquid TPCs, is that they provide a 3D image of particle tracks, which represent a useful tool to discriminate signal from background (the 'topological signature').

The signal of a $\beta\beta0\nu$ decay consists of two electrons originating from the same vertex, while the background comes essentially from the high energy gammas of the radioactive environment and detector components, which convert in the detection material, producing Compton and photoelectric electrons. If the energy of these electrons is close to the end-point of the $\beta\beta$ spectrum, falling within the window given by the energy resolution, they can be spuriously reconstructed as signal. However, in a gaseous TPC, signal and background can be differentiated exploiting the different patterns of their energy deposition in the gas. At a pressure of 15 bar, the two electrons emitted in a $\beta\beta0\nu$ decay leave a track of about 15 cm. An electron releases its energy interacting with the gas molecules at an almost fixed rate, until the end of its range, where it produces a larger energy deposition in a smaller region, as $dE/dx \propto 1/v^2$, where v is the speed of the electron, E its energy and x the travelled space. Therefore, the signature of a $\beta\beta0\nu$ event is a long track of constant energy with two larger energy depositions at the end points ('blobs'), while a background event shows only one blob at one extreme of the track. In Fig. 1, the distribution of the energy at the end-points of a track is shown, for Monte Carlo samples of $\beta\beta0\nu$ signal and background electrons produced by 2615 keV gammas from ^{208}Tl. It can be seen that the signal shows two similar blob energies, while the background has only one high energy blob and the other extreme has a significantly lower energy.

The first experiment that exploited the topological signature of a gaseous TPC in $\beta\beta0\nu$ searches was the Gotthard experiment, run by the the Caltech-Neuchâtel-PSI Collaboration in the 1990s, which used a $\sim$ 3.3 kg ^{136}Xe TPC at a pressure of 5 bar with multiwire read-out. It obtained an excellent signal efficiency of 68% for a background rejection of single electrons of 96.5%, via a visual scanning of the events [4]. However, the Gotthard TPC had a poor energy resolution, limited by the fluctuations in the avalanche gain and

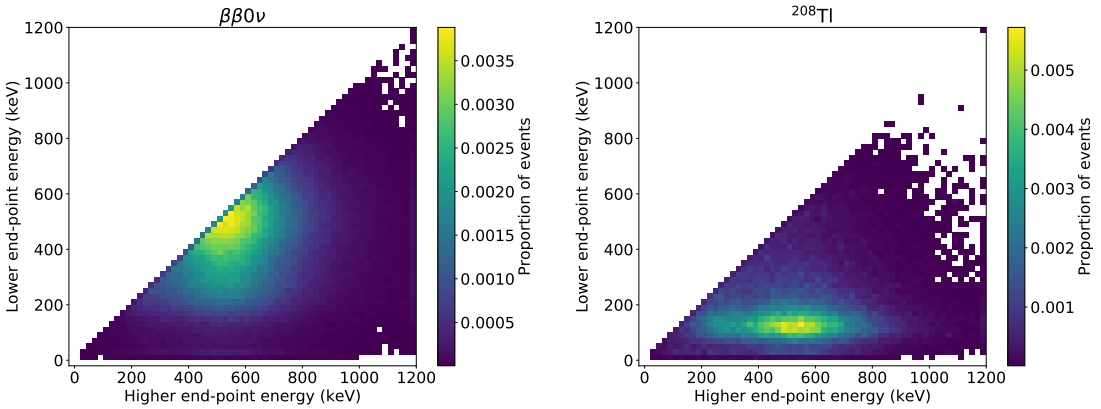

Figure 1. Distribution of the end-point energies of $\beta\beta0\nu$ (left) and ^{208}Tl (right) events for NEXT-100 simulation at 15 bar.

those introduced by the quenching of the scintillation light due to the gas mixture, which was used to reduce diffusion. Additionally, the quencher made the detection of the primary scintillation signal impossible, therefore preventing the z coordinate reconstruction and the rejection of background electrons coming from the cathode.

The NEXT Collaboration published a first proof of the power of the topological signature in an electroluminescent gaseous xenon TPC [5], using the NEXT-DEMO prototype, which contained 1.5 kg of natural xenon. In that work, events in the double escape peak of the 2.6-MeV gamma coming from ^{228}Th decay were used to mimic the signal, while the background consisted of events in the photoelectric peak of the high energy de-excitation gamma of ^{22}Na. A signal efficiency of 66.7 ± 0.9 (stat.)$\pm$ 0.3 (fit)% was measured, for a background acceptance of 24.3 ± 1.4 (stat.)%, in good agreement with Monte Carlo simulations. This study was limited by the small size of the NEXT-DEMO detector, in which the event selection tended to favour less extended events, with a more complicated reconstruction.

NEXT-White (NEW) is the first stage of the NEXT-100 detector, and deploys ∼5 kg of xenon in an active cylindrical volume of $\sim$ 53 cm of length and 40 cm of diameter, at 10 bar of pressure. Twelve photomultiplier tubes (PMTs) provide the energy measurement, while an array of 1-mm^2 silicon photomultipliers (SiPMs) is used for the particle track reconstruction. For a detailed description of the detector, see Ref. [6]. From October 2016 to early 2019, several runs of calibration and background measurements have been carried out with depleted xenon, and it has been demonstrated that an energy resolution of $\sim 1\%$ FWHM at the xenon $Q_{\beta\beta}$ ($\sim$ 2458 keV [7]) can be achieved [8, 9]. The first run with enriched xenon has started in February 2019, with the aim of measuring the two neutrino double beta decay spectrum.

In this work, calibration sources have been used in NEW to study the performance of the topological signature to discriminate signal from background. Also, a comparison between data and Monte Carlo has been developed, in order to extrapolate the results to

the $\beta\beta0\nu$ energy region.

The paper is organized as follows. In Sec. 2 the particle reconstruction employed in this study is described. Section 3 explains the selection applied on data and Monte Carlo events. In Sec. 4 the analysis procedure is presented and in Sec. 5 the results are discussed, as well as implications for the $\beta\beta0\nu$ region. Conclusions are drawn in Sec. 6.

2 Particle reconstruction

The electron tracks in NEW can be reconstructed by measuring the energy deposited along their path. The reference system used for the reconstruction is the natural one in a TPC, where the z axis follows the drift direction, the x and y axes are perpendicular to the z direction and the three coordinates together constitute a right-handed reference frame. Charged particles propagating in the xenon gas of the NEW detector release their energy through scintillation and ionization processes. While the scintillation light (S1), detected by the PMTs, gives the starting time of the event, the ionization charge is drifted by an electric field until it reaches the electroluminescence (EL) region, 6 mm wide, where a more intense electric field is applied and secondary scintillation (S2) is triggered. The S2 light is read both by the PMTs, which provide a precise measurement of the energy of the event, and by the SiPMs, placed a few mm away from the EL region, which are used to reconstruct the position. The detector triggers on the energy information read by the PMTs and provides PMT and SiPM waveforms in a buffer of a fixed size, which is always larger than the maximum possible drift time. The sampling time of the PMTs is 25 ns, while the SiPM charge is integrated every μs. Then, the S1 and S2 signals are searched for, using the sum of the individual PMT waveforms, and the events with one S1 and one or more S2 pulses are selected for track reconstruction.

The shape of the charge pattern on the SiPMs is affected on one hand by the longitudinal and transverse diffusion (~ 0.3 and ~ 1.1 mm/$\sqrt{\text{cm}}$ respectively [10]) and, on the other hand, by the spread of the light emission, which occurs along the 6 mm length of the EL region, and by the few mm distance of the SiPM plane from the emission region.

A first cut is performed on the SiPM collected charge to eliminate the dark current and the electronic noise. Time bins with less than 1 photoelectron (pe) charge are suppressed, after which the total integrated charge of a channel is required to be above 5 pe to be considered in the reconstruction. These requirements have been found to eliminate most of the SiPM noise, without affecting the signal. After this first cut, the SiPM charge is rebinned to 2 μs time sections (slices) and the charge pattern is examined for each slice. For each SiPM with charge higher than 30 pe a 3D hit is built, with x and y coordinates equal to the SiPM x and y positions and z coordinate equal to the difference between the time of the slice and the time of S1, multiplied by the drift velocity of the electrons in the gas. This large charge threshold has been found to be useful to eliminate the effects of the diffusion and light spread mentioned above: it removes the charge far from the center of the source of light, keeping the information on the position of the source. The energy measured by the PMTs in the same time slice is divided among the reconstructed hits, proportionally to the charge of the SiPMs used to determine their position.

Once the hits of an event are identified, they have to be grouped into sets corresponding to different particles. To this aim, a connectivity criterium is defined, according to the following procedure. The gas volume of the detector is divided into 3D pixels (voxels) with a fixed dimension and voxels that share a side, an edge or a corner are grouped into separated sets using a "Breadth First Search" (BFS) algorithm [11]. These sets of voxels are regarded as the particle tracks of the event. The BFS algorithm also identifies the end-point voxels of each track, defined as the pair of voxels with the longest distance between them, where the distance between any pair of voxels is the shortest path along the track that connects them. A maximum size of the voxels is fixed, but the actual voxel size varies event by event, being optimized according to the distribution of the hits in space. This optimization tries to avoid having voxels with only one hit on a border. In this work a maximum voxel size of $1.5 \times 1.5 \times 1.5$ cm^3 has been used, which gives the best performance in terms of topological discrimination of signal from background. A much finer voxelization would not help, since diffusion displaces the ionization electron position during the drift and the light spread due to the EL region produces a wide light pattern on the SiPMs, even for a point source. Moreover, as the distance between SiPMs is 1 cm, the current reconstruction does not allow for voxel sizes smaller than that value, since the minimum distance between hits is constrained to be also 1 cm.

In Fig. 2-*left* the reconstructed hits of an event produced by a ^{228}Th calibration source is displayed. A single electron track can be seen, accompanied by a separated energy deposition, possibly an electron produced by the conversion of a Bremsstrahlung photon. In the right plot the same reconstructed event is shown after voxelization.

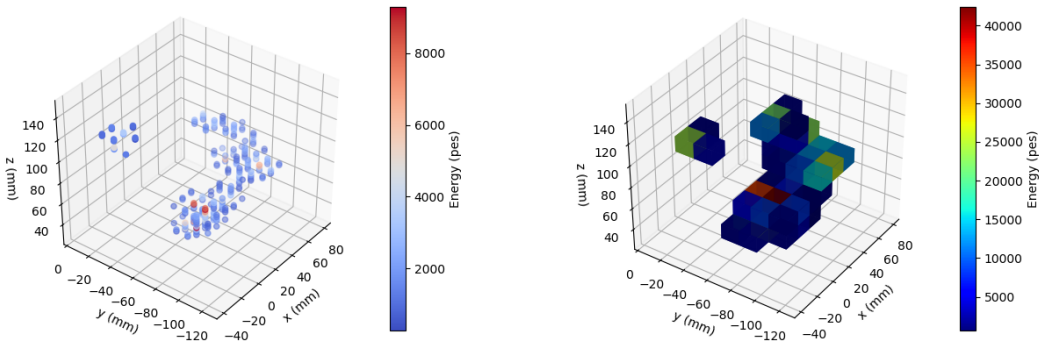

Figure 2. Example of reconstructed hits (left) and subsequent voxelization (right). This event was produced by a ^{228}Th calibration source.

3 Data and event selection

3.1 Data samples

The data sets used in this work have been acquired in January 2019, during the calibration runs of the NEW detector. A ^{228}Th source was placed on the top of the detector, inserted

in a feedthrough with a z position in the middle of the drift region. One of the thorium daughters, ^{208}Tl, decays producing a de-excitation gamma of 2.615 MeV, which can enter the active region of the detector and convert via pair production. The positron emitted in this process propagates in the gas in the same way as an electron and finally annihilates with an electron of a xenon atom, emitting two back-to-back 511-keV gammas. The energies of the electron and the positron, which are reconstructed as one track, form a peak at 1.593 MeV in the track energy spectrum (the double escape peak) and its topology is the same as that of a $\beta\beta0\nu$ event, in which two electrons originate from the same point. Therefore, this peak can be exploited to study the efficiency of the reconstruction algorithms and the cuts based on the topology signature, in order to estimate their performance on the $\beta\beta0\nu$ signal. From the continuum Compton spectrum of the 2.615-MeV gamma, a sample of tracks with the same energy as the double escape peak can be extracted, and used to estimate the efficiency of background rejection.

The detector gas pressure was set to 10.1 bar and the cathode and gate voltages to 30 kV and 7.7 kV, respectively, which gave a stable drift electric field of $\simeq$0.4 kV/cm and an EL reduced electric field of $\simeq$1.27 kV/(cm·bar). The drift velocity was very stable and it has been measured to be $\simeq$0.92 mm/μs. The electron lifetime was measured continuously using a ^{83m}Kr source diffused isotropically in the gas and the collected charge at the PMT plane was corrected for it (for a detailed description of the NEW calibration procedure, see Ref. [12]). The ^{83m}Kr source provides also a map of the geometric dependence of the PMT response to EL light, which was also used to correct the detected charge for geometric effects. After these corrections, a residual dependence of the energy on the length of the track in the z-dimension was found, in which the measured energy appeared to be lower for larger tracks. A linear fit was performed to model this dependence and used to correct it. For a more detailed description of this effect, see Ref. [9].

The energy of the events was calibrated using a quadratic interpolation of two peaks of the ^{228}Th spectrum, namely the 2615-keV gamma double escape peak and photopeak, and the 662-keV photopeak of a ^{137}Cs source placed in a lateral port. Both sources were in place at the same time and the trigger parameters were set in order to acquire both kinds of signal. In particular, the minimum charge of S2 was low enough as to include the ^{137}Cs photopeak. As explained in Ref. [9], a non-linearity is observed in the energy reconstruction of the events in the NEW detector, therefore a linear fit to the three peaks does not produce satisfactory results. Since the optimization of the energy resolution is not required in this analysis, and the results are obtained using the high energy part of the spectrum (the ^{208}Tl double escape peak and photopeak), a quadratic interpolation among these three peaks has been considered accurate enough.

A summary of the characteristics of each data set used in this work is presented in Table 1.

A complete Monte Carlo simulation of the decay of a ^{208}Tl source in the same conditions as the real detector was produced, to be compared with data. The particle propagation and their energy deposition in the detector are simulated using the *nexus* software [13], a simulation package based on Geant4 [14, 15]. Subsequently, electron diffusion and attachment, S1 and S2 light signal and their detection by PMTs and SiPMs are simulated, together

Run number	Duration (s)	Number of triggers
6818	91 248	525 243
6822	171 153	990 892
6823	74 943	425 009
6826	93 187	509 296
6828	74 233	432 215

Table 1. Summary of the data used in this work.

with a full electronics response, using the IC framework, a simulation and reconstruction package based on python and developed by the NEXT Collaboration. The outcome of the simulation is a set of waveforms, as for data, which passes through the same reconstruction procedure described in Sec. 2.

3.2 Event selection

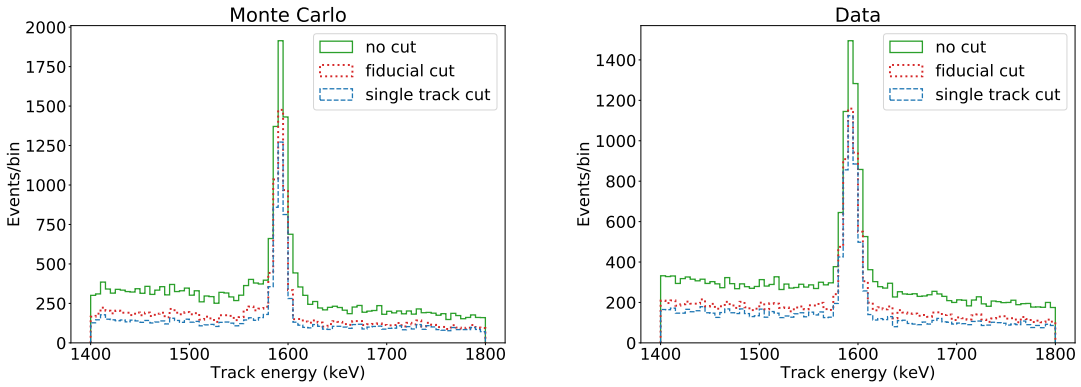

Figure 3. Distribution of the track energy in the region around the double escape peak before any cut and after the single-track and the fiducial cut (see text for details). Left: Monte Carlo, right: data.

After the reconstruction step, which provides a set of tracks for each event, a first fiducial filter is applied, in order to identify events with the correct energy in the double escape peak. Both data and Monte Carlo samples are required to be fully contained in a fiducial volume, defined as the volume contained within $\simeq$2 cm from all the borders of the drift region, namely R<180 mm, and 20 mm < Z < 510 mm. A track is considered fully contained if each one of its hits lies inside the fiducial volume. Subsequently, a second filter is applied, which requires that the events have a single track. This filter is found to clean up the region of the peak, eliminating, on one hand, the events with the emission of a bremsstrahlung or an X ray photon and on the other hand higher energy tracks which have been reconstructed erroneously as two or more tracks and where the energy of one of them falls in the region of interest. Removing multi-track events improves the energy resolution of the double escape peak and the modelling of the track energy distribution as a gaussian

plus an exponential function, as shown later. In Fig. 3 the track energy distribution is shown before and after these cuts, for Monte Carlo (*left*) and data (*right*). A last filter is applied during event selection, which ensures that the two blob candidates of a track (defined in the following section) do not overlap. At the energies of the ^{208}Tl double escape peak this requirement has little effect, rejecting less than 2% of tracks both in data and Monte Carlo.

4 Topological discrimination

4.1 Blob candidate definition

The aim of this work is to assess the performance of a cut on the energy of the end-points of the track, as a means to discriminate signal from background (the blob cut). For each track, two blob candidate energies are defined by summing the energy of the hits contained in a sphere of fixed radius centred on the end-points previously identified with the BFS algorithm, as explained in Sec. 2. It can happen that hits are included in the blob candidate that are far away from the extreme in terms of distance measured along the track, but have a short euclidean distance from it (as, for example, in the case of a winding track). In order to avoid this, only the hits belonging to the voxels that have a distance along the track shorter than the radius plus an allowance are considered. The allowance is needed because the voxel position is discretized, therefore an extra distance equivalent to the size of the voxel diagonal is added to the radius, only to select the voxels, to ensure that all the hits within the spheres are taken correctly into account. Once the voxel candidates are selected, only the hits belonging to those voxels and that have a euclidean distance shorter than the radius from the end-points of the tracks are considered for the blob candidates.

In Fig. 4 the energy distribution of the two blob candidates is shown for data and Monte Carlo, for tracks with energies in the ^{208}Tl double-escape peak. On the x and y axis, the energy of the higher energy blob candidate (from now on, *blob candidate 1*) and the energy of the lower energy blob candidates (*blob candidate 2*) are represented, respectively. A cut on the energy of *blob candidate 2* will be applied, to separate background from signal. Since the estimated fraction of signal-like and background-like events is similar in data and Monte Carlo, with a prevalence of the former ($74.6 \pm 1.5\%$ vs $25.4 \pm 0.3\%$ for Monte Carlo and $75.8 \pm 1.5\%$ versus $24.2 \pm 0.3\%$ for data), a direct comparison can be made of the mean value of the *blob candidate 2* energy. A difference of around 12% can be appreciated for *blob candidate 2*, where the Monte Carlo blob candidates are those with higher energy. The same amount of difference appears analyzing an energy region just at the right side of the double escape peak, where virtually zero signal-like events are present, namely between 1650 and 1700 keV, as can be seen in Fig. 5. Since in this region the *blob candidate 2* is genuinely the beginning of an electron track, one can infer that, at these energies, there exists a difference of $\sim$12% in the energy deposition at the beginning of the track, between Monte Carlo and data. The reason for this discrepancy is not completely understood, and it could be related with a difference in the length of the tracks, which appear to be slightly larger in data than in Monte Carlo.

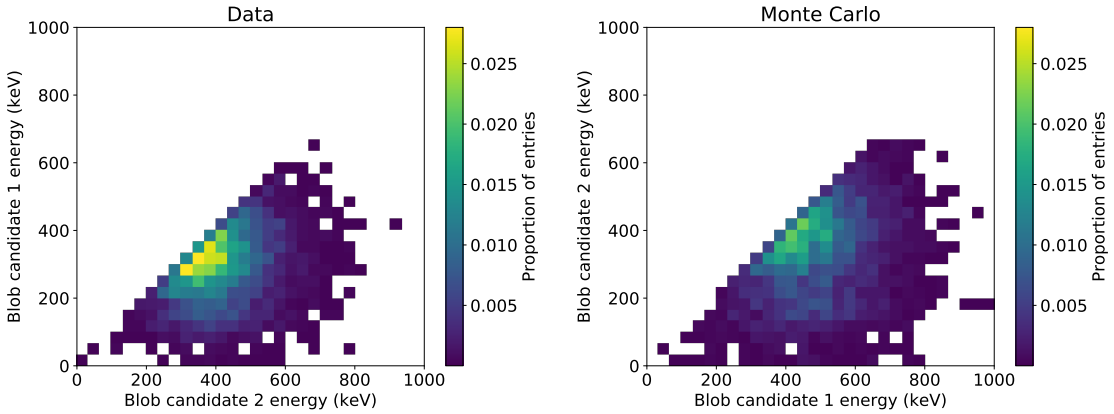

Figure 4. Distribution of the energies of *blob candidate 1* and *blob candidate 2* for data (left) and Monte Carlo (right).

4.2 Efficiency calculation

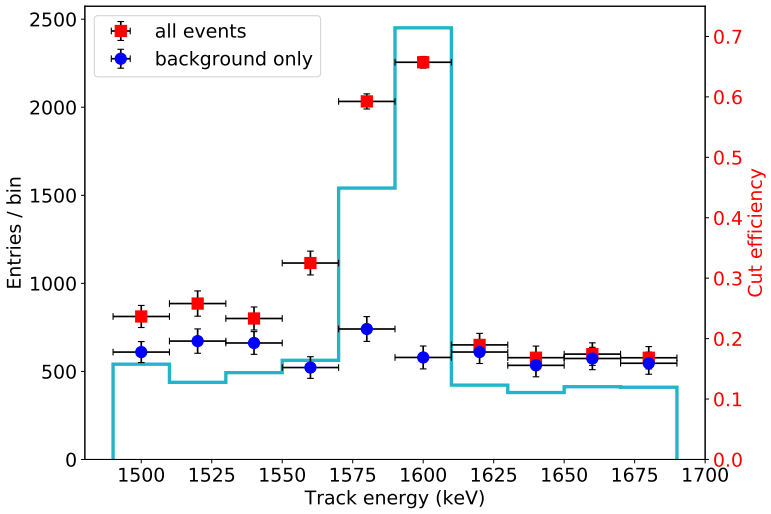

Figure 5. Blob cut efficiency for Monte Carlo, using the full sample and a sample of background-only events. The histogram represents the full sample of track energies and the points are the fraction of the total number of events passing the cuts for each one of the two samples.

In Fig. 5 the efficiency of the blob cut as a function of the track energy is shown for the full sample of selected events and for a sample where only background-like events are retained, where this selection is made using the true Monte Carlo information. The plot illustrates the fact that in the energy bins where a mixture of signal-like and background-like events are present, the total efficiency of the cut increases dramatically, while the efficiency of the background-like events stays constant.

To calculate the efficiency of the blob cut on double electron tracks, we need to identify a sample of pure signal-like and background-like events. Since the ^{208}Tl double escape peak region is populated by both electron-positron pairs and Compton electrons, a fit to a gaussian+exponential function is applied to the track energy spectrum of the events that pass the selection described in Sec. 3.2, to separate the two samples statistically. In fact, the electron-positron track energies are expected to be gaussianly distributed, with a mean at 1593 keV, which is the energy of the 2.615-MeV de-excitation gamma of ^{208}Tl minus the energy of the two 511-keV gammas originating from the positron annihilation. On the other hand, the single-electron tracks come from the Compton continuum of the 2.615-MeV gamma, which can be modelled as an exponential function.

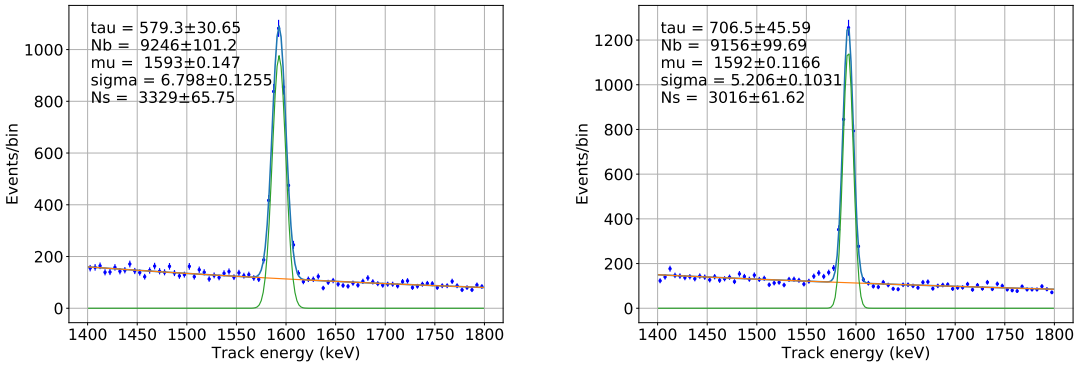

Figure 6. Energy spectrum and results of the gaussian+exponential fit for both data (left) and Monte Carlo (right).

A maximum likelihood unbinned fit is applied to the track energy spectrum, in the region between 1400 and 1800 keV, and the number of signal-like and background-like events in the double-escape peak region is calculated integrating the gaussian and exponential functions evaluated with the parameters obtained by the fit, in a pre-defined range between 1570 and 1615 keV. This range is large enough to contain virtually the whole gaussian peak for both data and Monte Carlo. The result of the fit is shown in Fig. 6. A variable threshold is applied on the energy of the two blob candidates, starting from 0 up to 500 keV. After each cut, the number of signal and background events is recalculated performing the fit on the energies of the tracks that pass the cut. The cut efficiency for both signal-like and background-like events is given by the ratio between the number of events of each type after the cut and the initial number of events of that type. In Fig. 7-*left* the signal efficiency and the background rejection (defined as the fraction of background events that do not pass the cut) are shown for each value of the threshold, for both data and Monte Carlo, which are in very good agreement. In order to choose the best value for the threshold, the following figure of merit is maximized:

$$\frac{\varepsilon}{\sqrt{b}} \tag{4.1}$$

where ε and b are the fraction of signal events and the fraction of background events passing the cut, respectively. This quantity is an estimator of the discrimination power

of the topological cut, since the sensitivity to the half-life of the $\beta\beta0\nu$ decay is directly proportional to the detector efficiency and inversely proportional to the square root of the rate of background [16]. In Fig. 7-*right*, this figure of merit is displayed as a function of the threshold. While the agreement between the efficiencies of data and Monte Carlo is good, the threshold that maximizes the figure of merit is lower in data than in Monte Carlo. This is a direct consequence of the mean *blob candidate 2* energy being lower in data, therefore a given cut for Monte Carlo will translate into a cut on data that will be lower by the same amount.

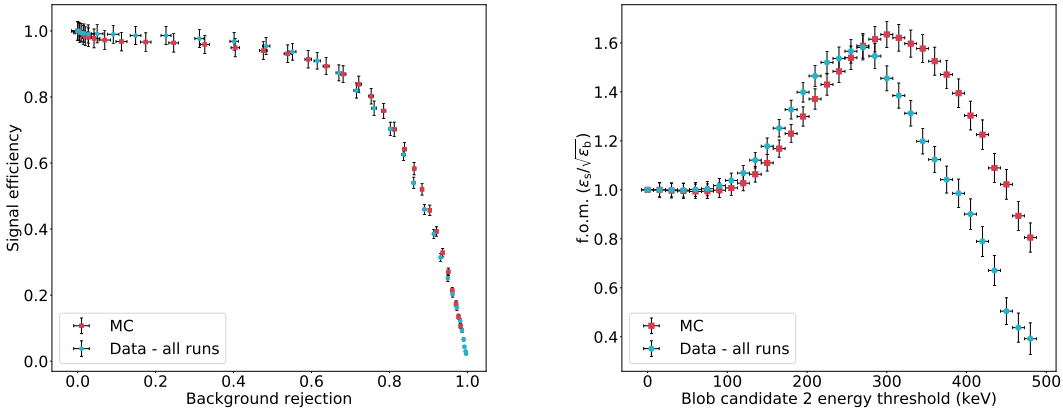

Figure 7. Left: Signal efficiency as a function of background rejection (proportion of background events removed from the sample by the blob cut), varying the required minimum energy of the *blob candidate 2*. Right: Figure of merit (defined in Eq. 4.1) as a function of the threshold on the energy of the *blob candidate 2*. In both figures, data and Monte Carlo simulation are shown.

4.3 Blob cut optimization

Several values for the blob candidate radius have been considered with the aim of maximizing the discrimination power of the topological cut and at the same time keeping the percentage of tracks with the two blob candidates overlapping to a minimum. The figure of merit used for this optimization is the same as in Eq.(4.1). In Fig. 8-*left* the fraction of tracks that present overlapping blob candidates is shown for both data and Monte Carlo for different radii, for events in the double escape peak, while in Fig. 8-*right* the figure of merit is shown as a function of the blob candidate radius and the value of the energy threshold on the *blob candidate 2*. A radius of 21 mm is chosen, since it provides a figure of merit among the highest ones and keeps the fraction of blob overlaps below 2% for both data and Monte Carlo.

5 Discussion

The value of the Monte Carlo *blob candidate 2* energy threshold that optimizes the performance of the blob cut is 300 keV and the efficiency obtained for pure signal-like events is

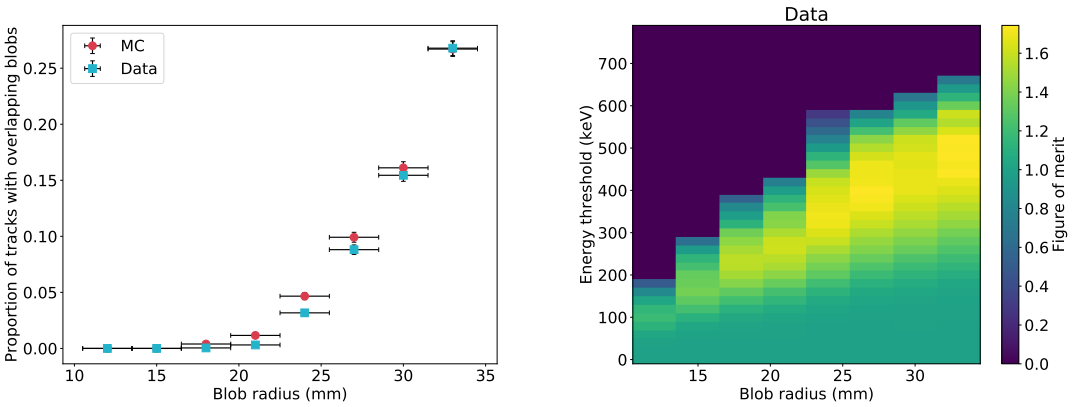

Figure 8. Proportion of events with overlapping blob candidates for data and Monte Carlo (left) and dependence of the figure of merit on the blob radius and the energy threshold on the *blob candidate 2* for data (right).

77.0 ± 3.8 (fit)% for a background acceptance of 21.3 ± 0.9 (fit)%. Given that the mean *blob candidate 2* energy is lower in data by about 12%, the value of the cut applied to data is reduced by the same amount, which gives a signal efficiency of 73.7 ± 5.0 (fit)% and a background acceptance of 21.6 ± 1.3 (fit)% for a cut of 263 keV. This result provides an improved topological discrimination compared to the measurement carried out in the NEXT-DEMO prototype, thanks to the larger dimensions of the NEXT-White detector, which allows for a better reconstruction of longer tracks, where the two end-points are well separated.

Having demonstrated the good agreement between data and Monte Carlo in the ^{208}Tl double escape peak region, it is possible to study the efficiency of the blob cut in the $\beta\beta0\nu$ region, with Monte Carlo simulations, and extrapolate the results to data. To this aim, two dedicated samples have been simulated, with the same detector conditions as the ^{208}Tl calibration source sample used in the double escape peak analysis. The first one is a sample of $\beta\beta0\nu$ decays of ^{136}Xe, uniformly distributed in the active volume, while the second one generated from nuclei of ^{208}Tl distributed in the teflon light tube that surrounds the active volume, which is one of the dominant contributions in the NEXT-White background model. The 2.615-MeV thallium de-excitation gamma produced in the decay can interact in the xenon through Compton effect, producing electrons with a continuous energy distribution in the region around the ^{136}Xe Q-value.

The same reconstruction, selection and analysis used for the ^{208}Tl double escape peak region are applied, within an energy window of 6 sigmas around the $\beta\beta0\nu$ peak (namely, 2435–2481 keV) and the curve of signal efficiency versus background rejection for the $\beta\beta0\nu$ region is shown in Fig. 9. In order to extrapolate to this energy region the threshold found for the ^{208}Tl double escape peak, one needs to compare the mean value of the energy of the beginning of the electron tracks at the two energy regions. The mean *blob candidate 2* energy of tracks with energies between 1650 and 1700 keV (a pure background sample,

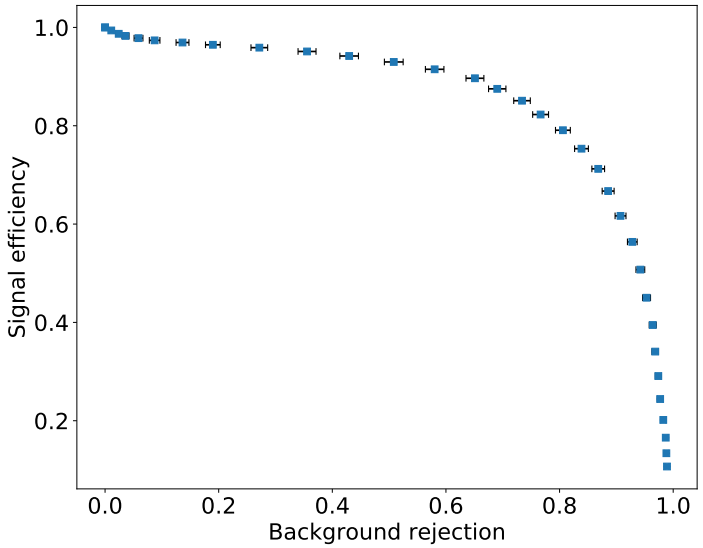

Figure 9. Signal efficiency as a function of background rejection, varying the required minimum energy of the *blob candidate 2*, in the $\beta\beta0\nu$ region.

as mentioned in Sec. 4.1) is around 212 keV, while the mean *blob candidate 2* energy of the ^{208}Tl sample in the energy region of the $\beta\beta0\nu$ peak is 196 keV. Translating this 7-8% relative difference to the optimal threshold of 300 keV found for the double escape peak region, a threshold of $\sim$ 277 keV is chosen for the comparison. With this threshold, a signal efficiency of 77.9 ± 0.1 (stat.)% is found, for a background acceptance of 17.7 ± 1.3 (stat.)%. The blob cut appears to perform slightly better at the $\beta\beta0\nu$ energies than at the lower energies of the ^{208}Tl double escape peak, which is expected, since the tracks are larger, and therefore the separation between their end-points is better defined.

6 Conclusions

In this work, the power of the topological discrimination of signal from background has been explored in the NEXT-White detector. Electron-positron pair tracks have been used to mimic the $\beta\beta0\nu$ signal, while single-electron tracks coming from Compton interactions, at the same energy, have been used as a background sample. The difference in the deposited energy at the beginning and at the end of an electron (or positron) track has been exploited to define a cut to separate signal from background, namely, a threshold on the lower energy extreme of a track. A threshold of 263 keV provides a signal efficiency of 73.7 ± 5.0 (fit)% for a background acceptance of 21.6 ± 1.3 (fit)%. This result improves on the one reported in Ref. [5], thanks to an improved track reconstruction, and also due to the larger dimensions of the detector.

The agreement of the blob cut performance between data and Monte Carlo simulation is very good, and therefore a study of the same cut has been carried out with Monte Carlo

to estimate the expected performance in the $\beta\beta0\nu$ energy region. A signal efficiency of 77.9 ± 0.1 (stat.)% is predicted, for a background acceptance of 17.7 ± 1.3 (stat.)%. The same analysis will be done with the simulation of the NEXT-100 detector geometry, at its operation pressure of 15 bar, to obtain a prediction for the search of $\beta\beta0\nu$ decay.

Acknowledgments

The NEXT Collaboration acknowledges support from the following agencies and institutions: the European Research Council (ERC) under the Advanced Grant 339787-NEXT; the European Union's Framework Programme for Research and Innovation Horizon 2020 (2014-2020) under the Marie Skłodowska-Curie Grant Agreements No. 674896, 690575 and 740055; the Ministerio de Economía y Competitividad of Spain under grants FIS2014-53371-C04, the Severo Ochoa Program SEV-2014-0398 and the María de Maetzu Program MDM-2016-0692; the GVA of Spain under grants PROMETEO/2016/120 and SEJI/2017/011; the Portuguese FCT under project PTDC/FIS-NUC/2525/2014, under project UID/FIS/04559/2013 to fund the activities of LIBPhys, and under grants PD/BD/105921/2014, SFRH/BPD/109180/2015 and SFRH/BPD/76842/2011; the U.S. Department of Energy under contracts number DE-AC02-06CH11357 (Argonne National Laboratory), DE-AC02-07CH11359 (Fermi National Accelerator Laboratory), DE-FG02-13ER42020 (Texas A&M) and DE-SC0017721 (University of Texas at Arlington); and the University of Texas at Arlington. DGD acknowledges Ramon y Cajal program (Spain) under contract number RYC-2015-18820. We also warmly acknowledge the Laboratori Nazionali del Gran Sasso (LNGS) and the Dark Side collaboration for their help with TPB coating of various parts of the NEXT-White TPC. Finally, we are grateful to the Laboratorio Subterráneo de Canfranc for hosting and supporting the NEXT experiment.

References

[1] M. Fukugita and T. Yanagida, *Baryogenesis Without Grand Unification*, *Phys. Lett.* **B174** (1986) 45.

[2] **EXO-200** Collaboration, J. B. Albert et al., *Improved measurement of the $2\nu\beta\beta$ half-life of ^{136}Xe with the EXO-200 detector*, *Phys. Rev.* **C89** (2014), no. 1 015502, [arXiv:1306.6106].

[3] **XENON** Collaboration, E. Aprile et al., *Dark Matter Search Results from a One Ton-Year Exposure of XENON1T*, *Phys. Rev. Lett.* **121** (2018), no. 11 111302, [arXiv:1805.1256].

[4] **Caltech-Neuchâtel-PSI** Collaboration, R. Luscher et al., *Search for $\beta\beta$ decay in Xe-136: New results from the Gotthard experiment*, *Phys. Lett. B* **434** (1998) 407–414.

[5] **NEXT** Collaboration, P. Ferrario et al., *First proof of topological signature in the high pressure xenon gas TPC with electroluminescence amplification for the NEXT experiment*, *JHEP* **01** (2016) 104, [arXiv:1507.0590].

[6] **NEXT** Collaboration, F. Monrabal et al., *The Next White (NEW) Detector*, *JINST* **13** (2018), no. 12 P12010, [arXiv:1804.0240].

[7] M. Redshaw, E. Wingfield, J. McDaniel, and E. G. Myers, *Mass and double-beta-decay Q value of Xe-136*, *Phys. Rev. Lett.* **98** (2007) 053003.

[8] **NEXT** Collaboration, J. Renner et al., *Initial results on energy resolution of the NEXT-White detector*, *JINST* **13** (2018), no. 10 P10020, [arXiv:1808.0180].

[9] **NEXT** Collaboration, J. Renner et al., "Results on energy resolution of the NEXT-White detector." in preparation.

[10] **NEXT** Collaboration, A. Simón et al., *Electron drift properties in high pressure gaseous xenon*, *JINST* **13** (2018) P07013, [arXiv:1804.0168].

[11] T. H. Cormen, C. Stein, R. L. Rivest, and C. E. Leiserson, *Introduction to algorithms*. McGraw-Hill Higher Education, 2nd ed., 2001.

[12] **NEXT** Collaboration, G. Martínez-Lema et al., *Calibration of the NEXT-White detector using* ^{83m}Kr *decays*, *JINST* **13** (2018), no. 10 P10014, [arXiv:1804.0178].

[13] J. Martín-Albo, *The NEXT experiment for neutrinoless double beta decay searches*. PhD thesis, Valencia U., IFIC, 2015.

[14] **GEANT4** Collaboration, S. Agostinelli et al., *GEANT4: A Simulation toolkit*, *Nucl. Instrum. Meth.* **A506** (2003) 250–303.

[15] S. Agostinelli et al., *Geant4 simulation toolkit*, *Nuclear Instruments and Methods in Physics Research Section A: Accelerators, Spectrometers, Detectors and Associated Equipment* **506** (2003), no. 3 250 – 303.

[16] J. J. Gómez-Cadenas et al., *Sense and sensitivity of double beta decay experiments*, *JCAP* **1106** (2011) 007, [arXiv:1010.5112].